Analysis of narrowband emission observed in the Saturn magnetosphere

J. D. Menietti,[1] S.-Y. Ye,[1] P. H. Yoon,[2] O. Santolík,[3,4] A. M. Rymer,[5] D. A. Gurnett,[1] and A. J. Coates[6]

[1] Narrowband emission is observed at Saturn centered near 5 kHz and 20 kHz and harmonics of 20 kHz. This emission appears to be in many ways similar to Jovian narrowband emission observed at higher frequencies. We analyze one example of this emission near a possible source region. In situ electron distributions suggest narrowband emission has a source region associated with electrostatic cyclotron harmonic and upper hybrid emission. Linear growth rate calculations indicate that the observed plasma distributions are unstable to the growth of electrostatic harmonic emissions. In addition, it is found that when the local upper hybrid frequency is close to $2 f_{ce}$ or $3 f_{ce}$ (f_{ce} is the electron cyclotron frequency), electromagnetic Z mode and weak ordinary (O mode) emission can be directly generated by the cyclotron maser instability. In the presence of density gradients, Z mode emission can mode-convert into O mode emission, and this might explain the narrowband emission observed by the Cassini spacecraft.

1. Introduction

[2] Our knowledge of planetary plasma waves and radio emission is filtered by our knowledge of terrestrial emissions. Earth orbiting satellites have revealed two general types of nonthermal emission, directly generated emission and mode-converted (indirect) emission. Auroral kilometric radiation (AKR) is one of the most intense terrestrial radio emissions and is directly generated by the cyclotron maser instability [*Gurnett*, 1974; *Wu and Lee*, 1979]. Terrestrial continuum emission and narrowband radio emissions are believed to be generated indirectly by mode conversion from intense electrostatic waves [*Gurnett*, 1975; *Jones*, 1976; *Melrose*, 1981]. Jovian decametric emission and Saturn kilometric radiation are believed to be directly generated by the cyclotron maser instability and are therefore counterparts of terrestrial AKR. Similarly, narrowband radio emissions are present at Jupiter (narrowband kilometric emission or nKOM) and at Saturn (narrowband emission) with similar characteristics to terrestrial narrow-band continuum emission and are believed to have a similar source mechanism.

[3] Narrowband emission observed at Saturn has many similarities to terrestrial narrow-banded nonthermal continuum emission. *Brown* [1973] and *Gurnett and Shaw* [1973] first reported terrestrial nonthermal continuum emission in a broad frequency range extending from ∼5 kHz to <100 kHz. *Gurnett and Shaw* [1973] and *Gurnett* [1975] proposed a source near the dawnside plasmapause, with a source mechanism associated with intense upper hybrid waves. *Kurth et al.* [1981] and *Kurth* [1982] described the details of the narrow-banded escaping component of continuum emission providing clear evidence of its narrow-bandedness associated with intense upper hybrid (UH) resonance emissions. These emissions are also believed to have a low-latitude source in the outer plasmasphere and in the magnetopause [*Morgan and Gurnett*, 1991]. The source mechanism of this continuum emission and planetary nonthermal continuum emission has been proposed to be a mode conversion process occurring near the dayside magnetopause and/or the nightside plasmapause near the equator. Both linear [e.g., *Jones*, 1976, 1988; *Budden*, 1980] and nonlinear [cf. *Melrose*, 1981; *Barbosa*, 1982; *Fung and Papadopoulos*, 1987; *Ronnmark*, 1983b, 1989] classes of mode conversion have been suggested as summarized by *Kurth* [1992]. All of these mechanisms involve electrostatic upper hybrid waves. In the linear mechanism upper hybrid waves refract (in a steep density gradient) to Z mode waves at a wave normal angle near 90°. Z mode waves can mode convert to O mode waves [cf. *Horne*, 1989, 1990]. The nonlinear mechanisms are described by the authors as more efficient than the linear conversion mechanism [*Ronnmark*, 1989]. For these

[1]Department of Physics and Astronomy, University of Iowa, Iowa City, Iowa, USA.

[2]Institute for Physical Science and Technology, University of Maryland, College Park, Maryland, USA.

[3]Faculty of Mathematics and Physics, Charles University, Prague, Czech Republic.

[4]Institute of Atmospheric Physics, Prague, Czech Republic.

[5]Applied Physics Laboratory, Johns Hopkins University, Laurel, Maryland, USA.

[6]Mullard Space Science Laboratory, University College London, Dorking, UK.

processes electrostatic upper hybrid waves coalesce with lower-frequency waves.

[4] Electrostatic $(n + 1/2) f_{ce}$ waves near the upper hybrid frequency, f_{UH}, are frequently observed in space plasmas and are often found to be associated with the observation of loss cone electron distributions at the source [*Kurth et al.*, 1979a, 1979b]. *Ronnmark et al.* [1978] have shown that wave growth rate maximizes when $(n + 1/2) f_{ce} \sim f_{UH}$ due to the nonconvective nature of the instability. Auroral roar emission is left-hand ordinary (*L-O*) mode emission observed by ground-based receivers at frequencies from $\sim 0.03-30$ MHz. These are narrow-banded emissions that are interpreted as emissions near the first and second harmonics of f_{ce}. In explaining the generation of terrestrial auroral roar, *Yoon et al.* [1996, 1998] have shown that the growth rates of *Z* mode are greatly enhanced when $f_{UH}^2 = f_{ce}^2 + f_{pe}^2 = (n f_{ce})^2$, where $n = 2$ and 3. This *Z* mode can escape into free space by a linear mode conversion into ordinary (*O*) or whistler mode [e.g., *Ellis*, 1956]. *Willes et al.* [1998] investigated a competing theory of nonlinear coalescence to explain the conversion of *Z* mode to a freely propagating mode (cf. *Melrose* [1991] applied to solar radio emission).

[5] Jovian narrow-band kilometric (nKOM) radio emission was first reported from the Voyager radio emission data [*Warwick et al.*, 1979; *Kaiser and Desch*, 1980]. The emission is characterized by its obvious narrow band (~ 50 kHz) and its relatively smooth morphology at frequencies centered typically near $100-300$ kHz. *Daigne and Leblanc* [1986] reported the emission to be polarized in the left-hand circular (LHC) mode when observed by Voyager from the northern magnetic hemisphere and RH polarized when observed from the southern. Thus it is consistent with *O* mode emission and similar to terrestrial continuum emission [*Gurnett*, 1975]. A number of theoretical models for the generation of nKOM currently exist [cf. *Jones*, 1987, 1988; *Fung and Papadopoulos*, 1987].

[6] The first detections of narrowband radio emission from Saturn were made by Voyager [*Gurnett et al.*, 1981; *Scarf et al.*, 1982]. Voyager 1 observed a band of emission near 5 kHz observed between about 3.25 R_S and 58 R_S. The inferred polarization of the emission was L-O mode. *Ye et al.* [2009] have recently presented an extensive survey of narrowband emissions observed in the Saturn magnetosphere by the Cassini RPWS instrument, primarily at frequencies near 5 kHz and near 20 kHz and sometimes harmonics separated by the local cyclotron frequency. The emission is observed most intensely associated with storms of Saturn kilometric radiation and then is seen each rotation. The typical bandwidth is $1-3$ kHz. *Ye et al.* [2009] have identified the electromagnetic emission as ordinary (*O*) mode. They present direction finding results supported with observations that locate the sources of the emission off the magnetic equator near the intersection of the surface of f_{ce} and the surface of plasma frequency where $(n + 1/2) f_{ce} \sim f_{UH}$. The emissions originate from the northern and southern edges of Saturn's plasma torus at $L \sim 7$ to 10 for 5 kHz or $L \sim 4$ to 7 for 20 kHz emission. These locations are consistent with the hypothesis that the emission is similar to continuum emission observed at Earth [cf. *Gurnett and Shaw*, 1973; *Morgan and Gurnett*, 1991] and at Jupiter [*Gurnett et al.*, 1983]. *Wang et al.* [2008] summarize the observations of narrowband radio emissions by Cassini and

examine the possible association of narrowband radio emissions with a revolving plasma cloud detected by the Magnetospheric Imaging/Ion and Neutral Camera (MIMI/INCA) instrument on board Cassini.

[7] In this paper we examine in some detail an example of narrowband emission observed by Cassini at Saturn with center frequency near 10 kHz. The example is associated with electrostatic cyclotron harmonic (ECH) emission and probable upper hybrid waves. We determine nonlinear fits to in situ particle observations and use a linear dispersion solver to calculate the growth rate of the ECH emissions. We then apply the cyclotron maser instability to calculate the growth rates for both the *Z* mode and *O* mode. The results indicate that the *Z* mode growth rate is many orders of magnitude higher than the *O* mode. We speculate on how *O* mode narrowband emission may be generated by mode conversion.

2. Instrumentation

2.1. RPWS

[8] The Cassini Radio and Plasma Wave Science (RPWS) instrument measures oscillating electric fields over the frequency range 1 Hz to 16 MHZ and magnetic fields in the range 1Hz to 12 kHz [cf. *Gurnett et al.*, 2004]. The instrument uses 3 nearly orthogonal electric field antennas and 3 orthogonal magnetic search coil antennas, providing a direction-finding capability. There are 5 receiver systems: the high-frequency receiver (HFR) covering 3.5 kHz to 16 MHZ; the medium frequency receiver (MFR) covering 24 Hz to 12 kHz; a low-frequency receiver (LFR) covering 1 Hz to 26 Hz; a 5-channel waveform receiver which operates in either a $1-26$ Hz or 3 Hz–2.5 kHz mode; and a high-resolution wideband receiver (WBR) that covers two frequency bands, 60 Hz to 10.5 kHz and 800 Hz to 74 kHz. The data presented in this study are measured by the HFR and MFR.

2.2. ELS

[9] The Cassini Plasma Spectrometer (CAPS) is composed of three sensors: the electron spectrometer (ELS), the ion beam spectrometer (IBS), and the ion mass spectrometer (IMS). Of importance in this study is the ELS which contains an 8-detector fan array in a single plane. Each detector has a $5.2° \times 20°$ field of view for a total in-plane field of view of $160°$. The instrument measures electron energy from 0.6 eV to 28,250 eV over a period of 2 seconds with a resolution of $\Delta E/E = 0.17$ [cf. *Young et al.*, 2004].

3. Analysis

3.1. Observations and Wave Growth Rate Analysis

[10] As explained by *Ye et al.* [2009] the Saturn NB emissions observed most frequently near 20 kHz have source regions that probably lie on the northern and southern edges of the plasma density torus at Saturn. These are best observed during Cassini orbits that extend to higher latitudes. We have isolated an example of this type of emission near a fortuitous encounter by Cassini of the probable source region on 24 April (DOY 114) 2007. At the time, the spacecraft was in a high-inclination orbit, having crossed the magnetic equator proceeding southward
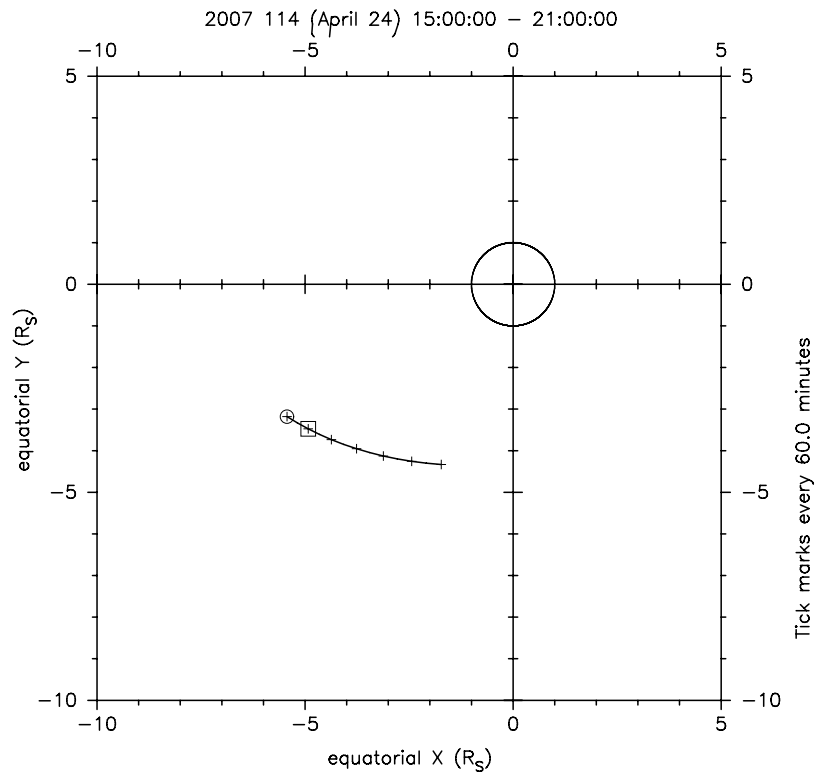
MENIETTI ET AL.: NARROWBAND EMISSION AT SATURN

2007 114 (April 24) 15:00:00 − 21:00:00

Figure 1a. A portion of the Cassini trajectory is shown in Saturn solar equatorial (SSQ) coordinates in the x-y plane.

at a radial distance of about 6 R_s and local time of about 3 hours. In Figure 1a we show a plot of a portion of the orbit in the x-y plane (Saturn solar equatorial coordinates) where +x is toward the sun in the Saturn-sun plane, and +z is along the northward spin axis of Saturn. Figure 1b shows this portion of the orbit in the ρ-z plane, where $\rho = (x^2 + y^2)^{1/2}$.
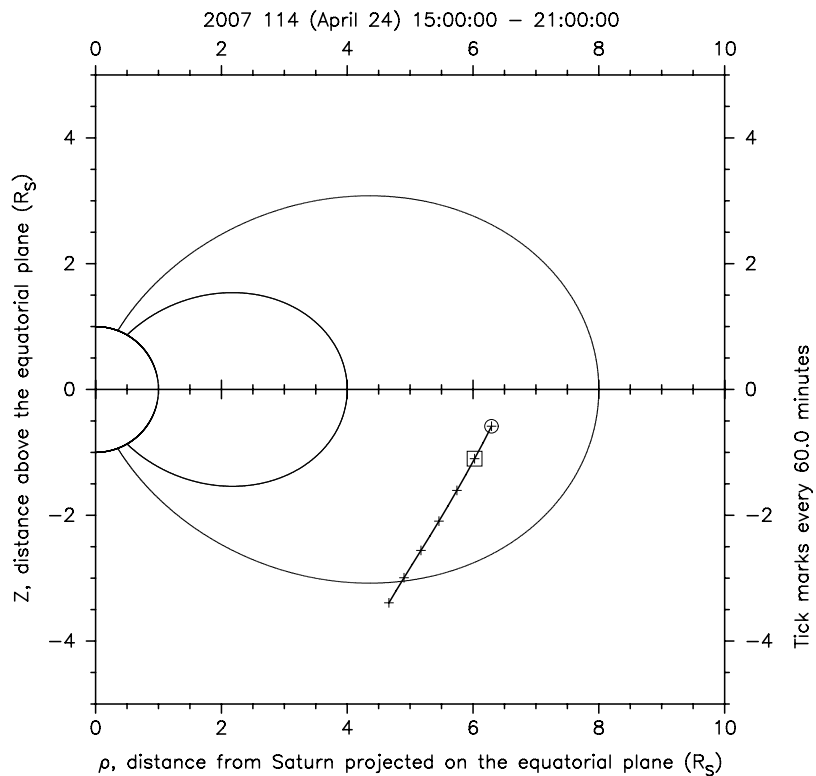
2007 114 (April 24) 15:00:00 − 21:00:00

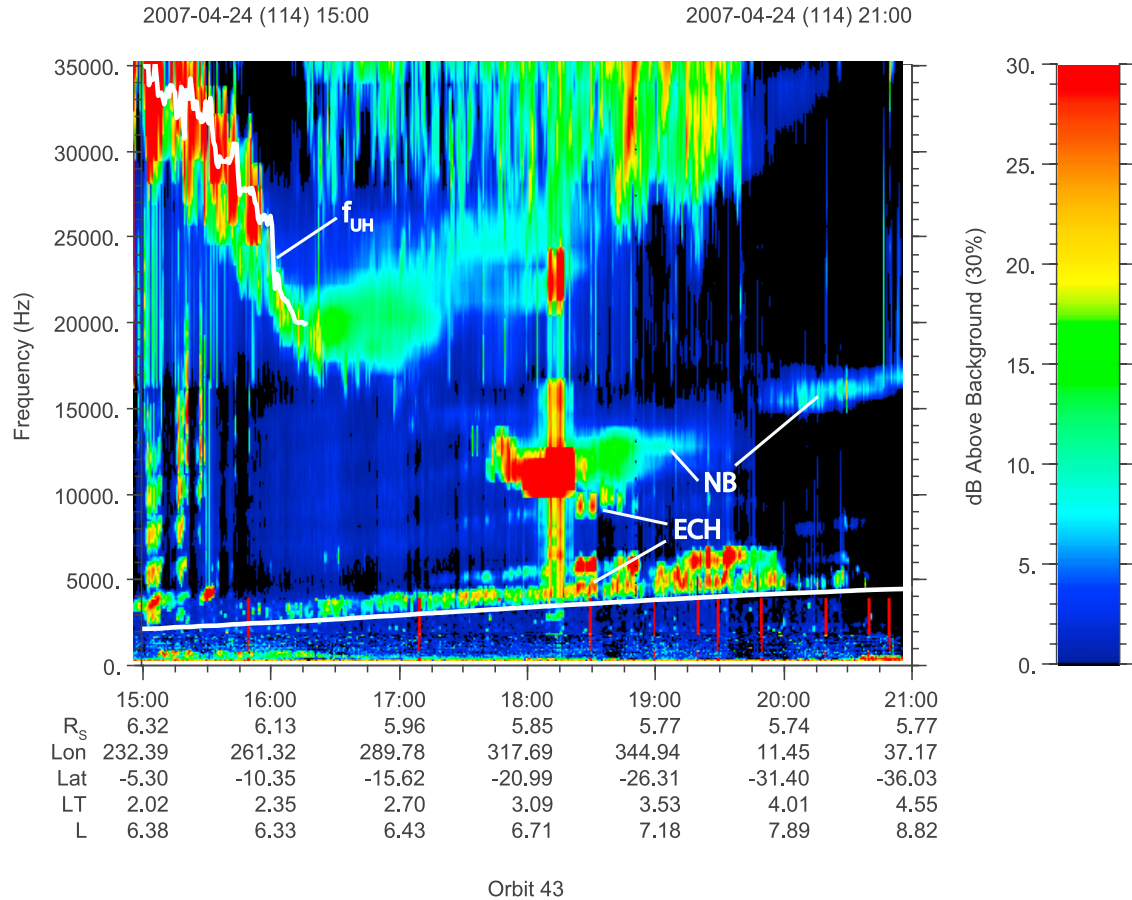**Figure 1b.** The same portion of the Cassini trajectory is shown in the ρ-z plane.

Figure 1c. A frequency versus time wave spectrogram for day 114 of 2007 for the time interval 1500 to 2100 UT. The frequency axis is linear, ranging from 0 to 35 kHz. The white line near the bottom of the plot indicates f_{ce}, while the more jagged white line above is f_{UH}. Narrowband (NB) emission and electrostatic cyclotron harmonics (ECH) are indicated.

[11] In Figure 1c we display the wave spectrogram for day 114 of 2007 for the time interval 1500 to 2100 UT. The frequency axis is linear ranging from 0 to 35 kHz. The white line near the bottom of the plot indicates f_{ce}, while the more jagged white line above depicts f_{UH}. The sharply decreasing value of f_{UH} indicates the proximity of a steep density gradient. Narrowband emission (NB) is seen indicated by the arrows. A possible source region of the narrowband emission is identified near 1745–1840 over the frequency range $10 < f < 12$ kHz. For reasons that will become clear later we believe this emission is a mixture of Z and O mode. The emission just above f_{ce} is electrostatic electron cyclotron emission and probably a harmonic emission (indicated with arrows). We show a close up of the region near a probable source region of narrowband emission in Figure 2, now with color bar indicating calibrated electric field spectral density. Z mode emission has an upper cutoff near f_{UH} and O mode has a lower cutoff near the plasma frequency (f_p). A feature identified as upper hybrid emission is indicated in Figure 2 near 1830 with an upper cutoff near 11.8 kHz. We estimate a slightly smaller value of $f_{UH} = 11.6$ kHz at 1834:30, where growth rate analysis will be conducted as discussed below. At this time $f_c = 3640$ Hz, so we calculate $f_p = 11.03$ kHz and $f_z = 9357$ Hz, where the latter is the low-frequency cutoff of Z mode, $f_z = \frac{1}{2}\left(\sqrt{f_c^2 + 4f_p^2} - f_c\right)$.

These values are consistent with independent determinations of f_p using plasma wave sounder data (P. Canu, private communication, 2008). A shift of f_p by ±1 kHz has almost no effect on the growth rate analysis discussed below.

[12] To confirm these wave identifications we show in Figure 3a the apparent circular polarization measurements for this emission as calculated from the RPWS instrument, over a time interval from 17.0 hours to 20.0 hours on day 114. In Figure 3a we show the region identified as Z mode and O mode narrowband emission. Apparent polarization recorded by RPWS in the 2-antenna mode refers to the polarization relative to the antenna plane, and assumes a direction of arrival perpendicular to the antenna plane (see *Fischer et al.* [2008] and *Ye et al.* [2009] for details). We note that the emission labeled Z mode and O mode changes apparent circular polarization from red to blue near 1830 UT. The polarization of O mode emission is left handed, while the Z mode in the cold plasma approximation for $f_p/f_c > 1$ and $f > f_p$ is extraordinary and propagation at wave normal angle of $\theta = 0$ is not possible [cf. *Gurnett and Bhattacharjee*, 2005; *Benson et al.*, 2006]. For $f_z < f < f_p$ the polarization of the mode is LHC at $\theta = 0$, and the wave is extraordinary at $\theta = 90°$. Since the Saturn Kilometric Radiation (SKR) is known to be generated as right-hand circular polarization (RCP), and at this time appears strongly red (~+1 on the

2007-04-24 (114) 17:30   2007-04-24 (114) 19:30
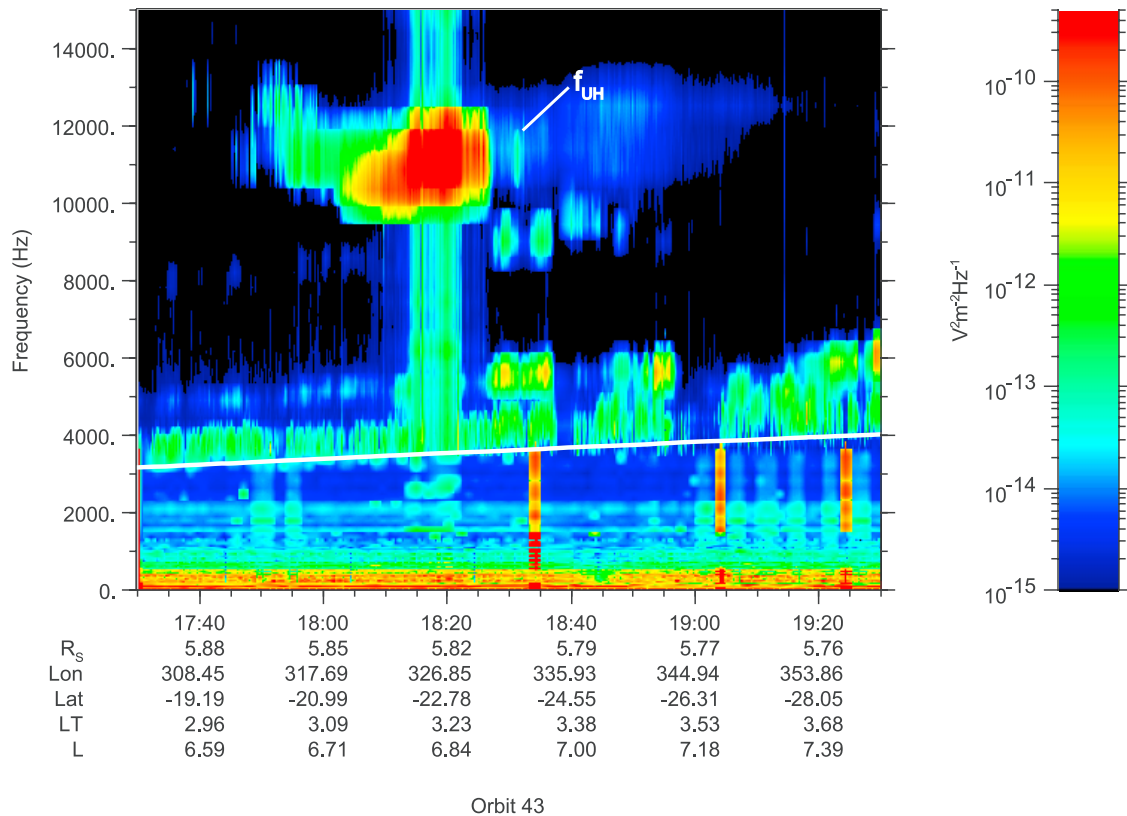

Orbit 43

Figure 2. A calibrated wave spectrogram showing a close-up of the region near a probable source region of narrowband emission.

color bar; data not shown here), we expect the left-hand circular polarization of O mode to appear blue on the spectrogram. We interpret the transition from red to blue to indicate that the Cassini spacecraft travels through the source region thus experiencing wave vectors, k, that

reverse direction relative to the local magnetic field producing a reversal of the apparent polarization, even though the actual polarization remains LCP. This is schematically shown in Figure 3b, where $\mathbf{k} \cdot \mathbf{B} < 0$ before the spacecraft encounters the source region, and $\mathbf{k} \cdot \mathbf{B} > 0$ after. The
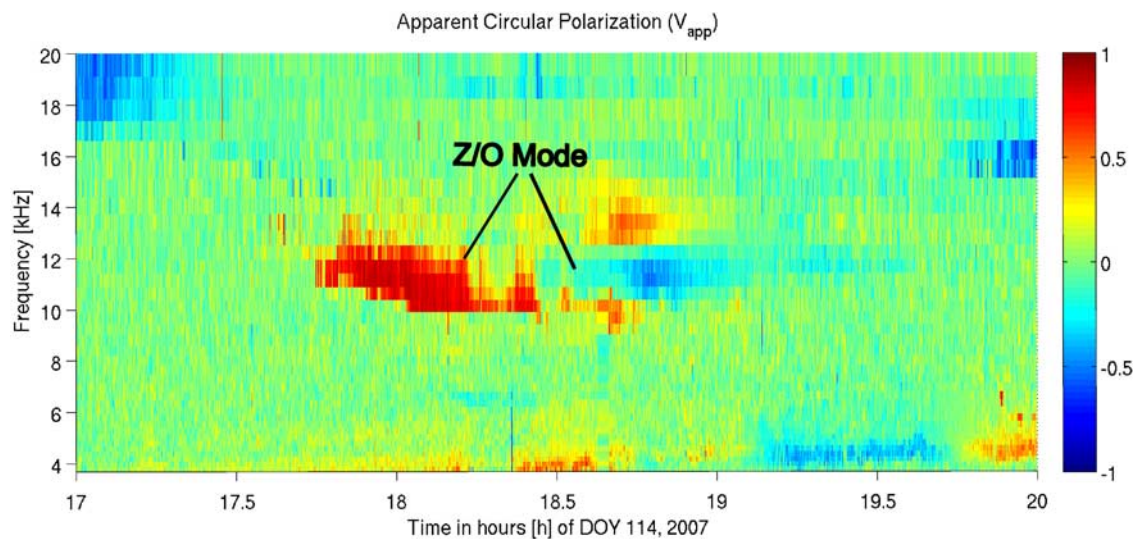

Figure 3a. Apparent circular polarization measurements as calculated from the RPWS instrument over a time interval from 17.0 h to 20.0 h on day 114. We show the region identified as Z mode and O mode narrowband emission.
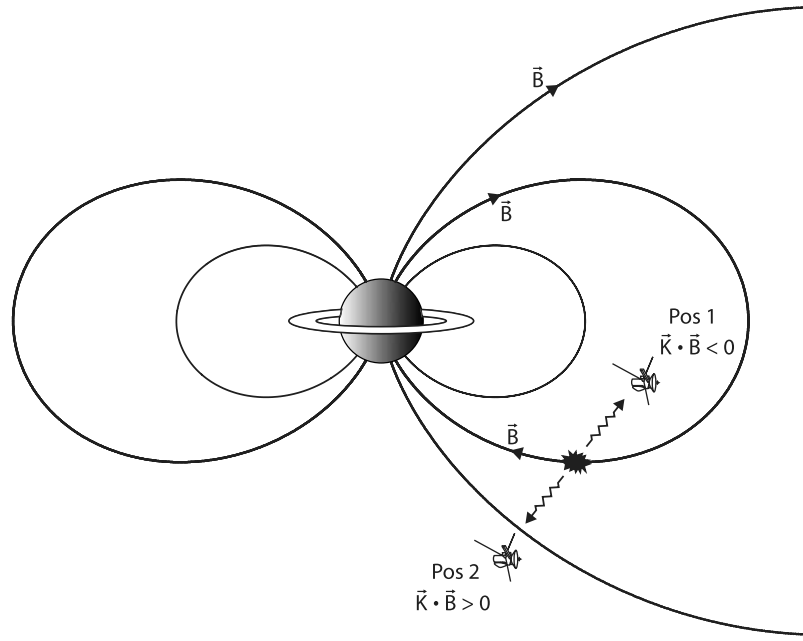
Figure 3b. A schematic diagram depicting the spacecraft at position 1 receiving emission from an NB source region with apparent left-hand circular polarization ($\mathbf{k} \cdot \mathbf{B} < 0$). After the spacecraft passes through the source region the apparent polarization changes to right-hand circular ($\mathbf{k} \cdot \mathbf{B} > 0$) even though the actual polarization of the NB emission does not change.

apparent reversal of polarization is interpreted, then, as evidence that the spacecraft traverses the source region.

[13] To investigate the generation mechanism of these waves we require the electron phase space density (PSD) distribution. At this time the ELS instrument was only viewing in one hemisphere covering an approximate range of pitch angles $100.7° < \alpha < 176.34°$. Since the spacecraft is located at low L-shells ($L < 7$) and most probably closed field lines [*Connerney et al.*, 1983], we have assumed that the data are gyrotropic and can also be mirror-reflected to the supplemental range of pitch angles, $180° − \alpha$. In Figure 4 we show a contour of the electron PSD for the time interval 1834:28–1834:30 UT, assuming the reflection of the data as described. The plot includes data for pitch angles within about 3.7 degrees of the magnetic field line, and we observe a loss cone for pitch angles less than about 20 degrees for $|V_{\parallel}| > 1 \times 10^7$ m/s. In Figure 5 we plot the electron PSD for $E < 568$ eV, showing a distinctive electron beam with a center near $|V_{\parallel}| = 4 \times 10^6$ m/s.

[14] We have fitted the observed ELS electron distribution function contours using a sum of bi-Maxwellians as follows

$$f_s(v_\perp, v_\parallel) = \sum_S \left(\frac{n_s}{\pi^{\frac{3}{2}} w_{\perp s}^2 w_{\parallel s}}\right) \left[(1 - \Delta_s)e^{-\frac{v_\perp^2}{w_{\perp s}^2}} + \frac{\Delta_s}{(1 - \beta_s)}\right.$$
$$\left. \cdot \left(e^{-\frac{v_\perp^2}{w_{\perp s}^2}} - e^{-\frac{v_\perp^2}{\beta_s w_{\perp s}^2}}\right)\right] e^{-\left(\frac{(v_\parallel - v_{ds})^2}{w_{\parallel s}^2}\right)} \quad (1)$$

where $v_\parallel$ and $v_\perp$ are the particle velocities parallel and perpendicular to the magnetic field, respectively; $w_\parallel$ and $w_\perp$ are the parallel and perpendicular thermal velocities,

respectively; v_d is the parallel drift velocity. The parameters Δ and β describe the depth and width of the model loss cone, respectively, and subscript "s" refers to the plasma populations or species, such as cold, energetic, etc.

[15] The nonlinear least squares fit to the electron PSD of Figures 4 and 5 using the functional form of equation (1) assumes seven populations of plasma: six electron distributions and a cold plasma ion distribution. The observed electron distribution warrants these model populations. The electron populations include a dominant (density) core plasma, a mid-energy warm plasma, an energetic warm plasma, a low-density, cool, electron beam traveling both directions along the magnetic field line, and a very cold isotropic electron background plasma. The ions are assumed to be a cold plasma background.

[16] The total density of the plasma was fixed by observations of the local upper hybrid resonance at the time, $f_{UH} = 11.6$ kHz. In Table 1 we present the fitting parameters determined for 24 April 2007, 1834:28–1834:30 UT. An overplot of contours of PSD determined from the data and from the model is presented in Figure 6.

[17] To determine roots of the dispersion equation and to calculate the growth rate of the electrostatic plasma waves resulting from the model distribution function, we have used a modification of a warm plasma dispersion solver [cf. *Santolik and Parrot*, 1996], based on the susceptibility tensor calculated by the "waves in homogeneous, anisotropic multicomponent plasmas" (WHAMP) code [cf. *Ronnmark*, 1983a]. The solver also includes a cold plasma susceptibility tensor, which we used for the background ion component.

[18] Roots of the dispersion equation and growth rate calculations of the plasma waves obtained from the model distribution function using this code are presented in Figure 7. Growth is seen for fundamental emission
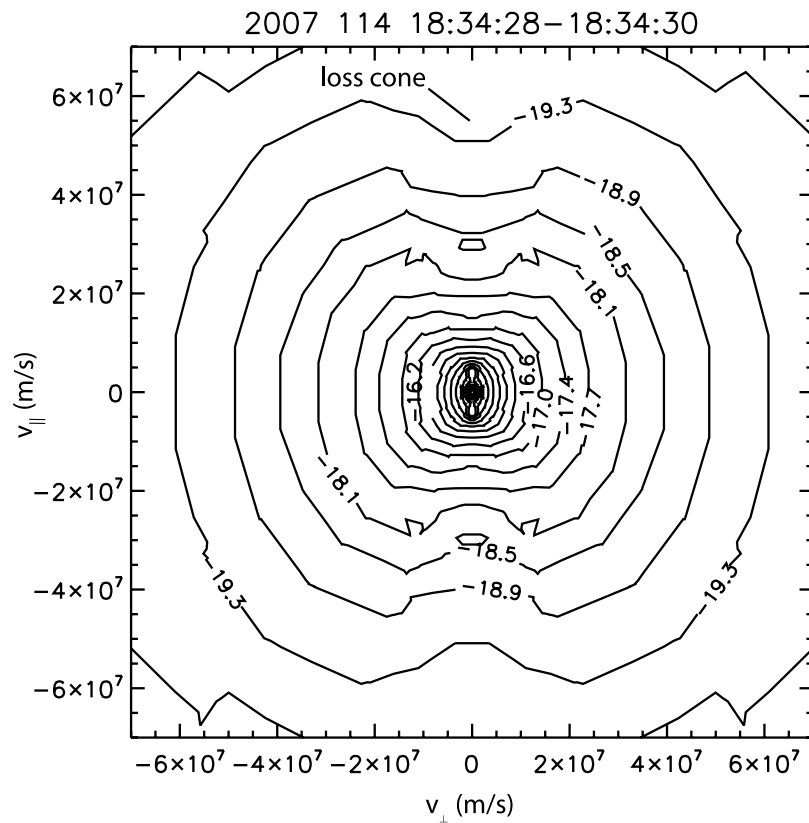
Figure 4. Contour of the electron distribution for the time interval 1834:28 to 1834:30 UT. The data have been reflected about a pitch angle of 90 degrees as described in the text. The contour levels are in units of s^3/m^6.
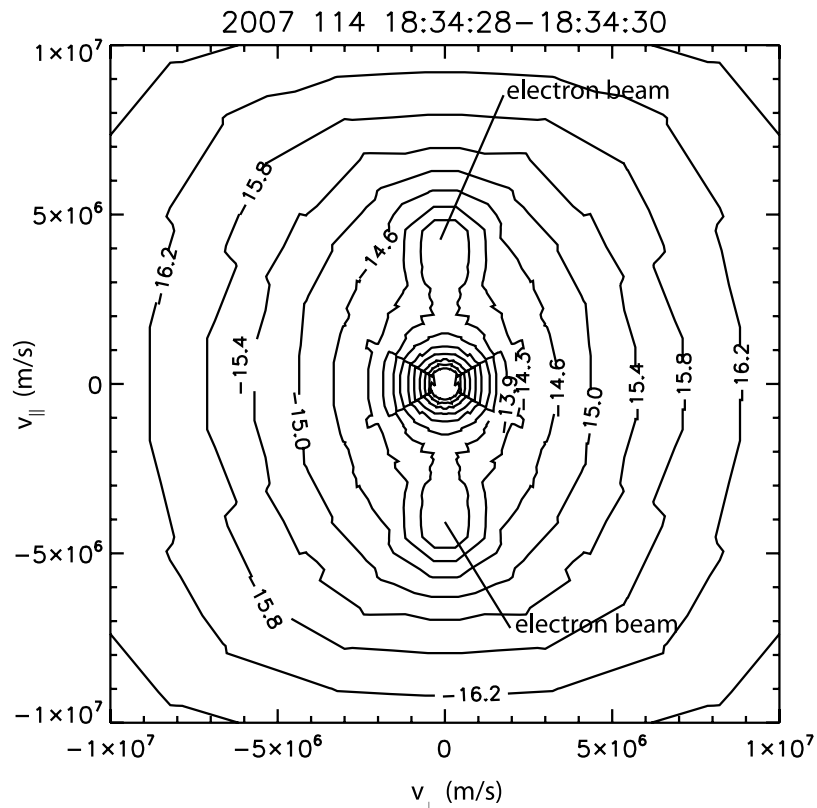
Figure 5. A close-up of the inner region of Figure 4 showing the electron phase space density for $E < 568$ eV and a distinctive electron beam with a center near $V_{\parallel} = \pm 4 \times 10^6$ m/s.

Table 1. Plasma Distribution Fitting Parameters

	Density[a] (%)	$W_\parallel$ (eV)	$T_\perp/T_\parallel$ (eV)	V_d (eV)	Δ	β
Cold background	2.0	0.063	1.0	0	1.0	0.0
Core	58.5	83.19	0.568	0	1.0	0.0
Mid-energy	22.0	386.2	1.23	0	1.0	0.0
Energetic	11.5	4677.	1.134	0	0.187	0.0167
Beam-dist.	3.0	6.079	0.464	42.42	1.0	0.0
Beam-dist.	3.0	−6.079	0.464	42.42	1.0	0.0
Cold ions	100	—	—	—	—	—

[a]Total density is 1.508 cm^{-3}.

(Figure 7a) and harmonic near 9 kHz (Figure 7b) at the approximate frequencies and bandwidths of the observations. For the fundamental emission we show results for emission near peak wave growth which occurred at a wave normal angle, $\theta = 87.5°$ (solid). We also show wave growth at near minimum wave normal angle $\theta = 55.5°$ (dotted), which produces a weaker but a more broadbanded emission. Figure 7b shows the results for emission near peak growth centered around 9 kHz for $\theta = 88.0°$. A weak growth for upper hybrid/Z mode emission is also found but not shown, and will be discussed in detail using a semirelativistic code in the next section. Although an intense narrow-banded emission is observed centered near 5500 Hz (see Figure 1), no wave growth for this frequency range was found in the linear dispersion analysis. We hypothesize that this emission, which falls between harmonics of f_c, may be propagating from a nearby source

region. The calculated and model bandwidths of the emission are listed in Table 2. The bandwidths can be extended at reduced growth rate by extending the range of wave normal angles ($\Delta\theta$) in the calculations as seen in row 2 of Table 2. The loss cone of the mid-energy plasma is the free energy source for the EC fundamental emission, harmonic, and Z mode/UH emission. Absence of the counterstreaming beams has almost no effect on any of these emissions.

[19] As mentioned above, for this time period we are also fortunate to have polarization measurements from the RPWS instrument, so that Z mode and O mode emission can be better identified. Growth rate calculations of these emissions require a semi-relativistic treatment, which is beyond the limitations of a linear nonrelativistic code. In the next section we treat these emissions using an analytical approach based on the work of *Yoon et al.* [1996, 1998].
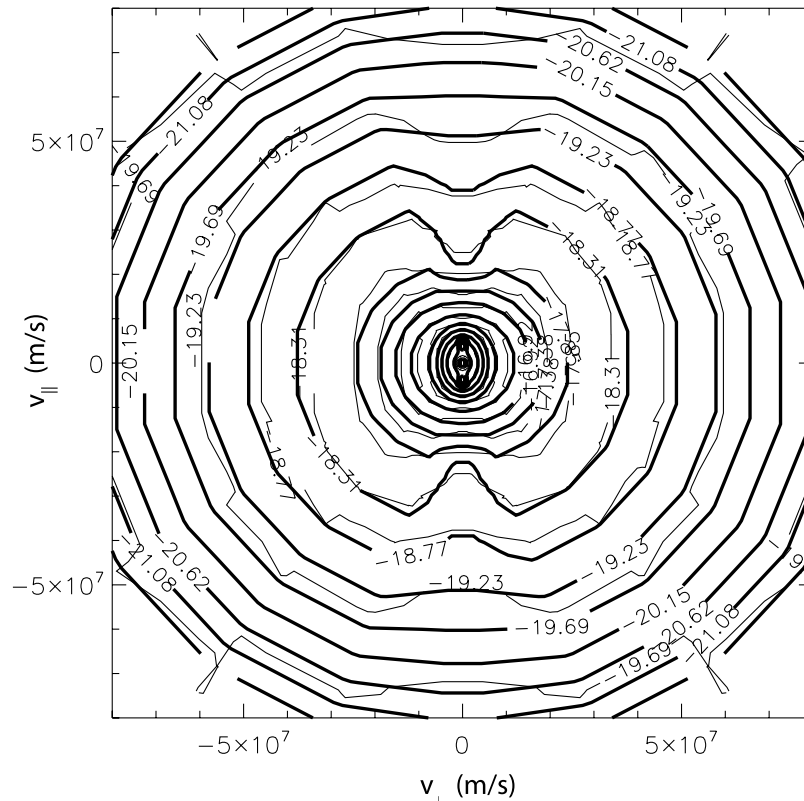

Figure 6. An overplot of contours of PSD determined from the data and from the model described by equation (1) with parameters from Table 1.
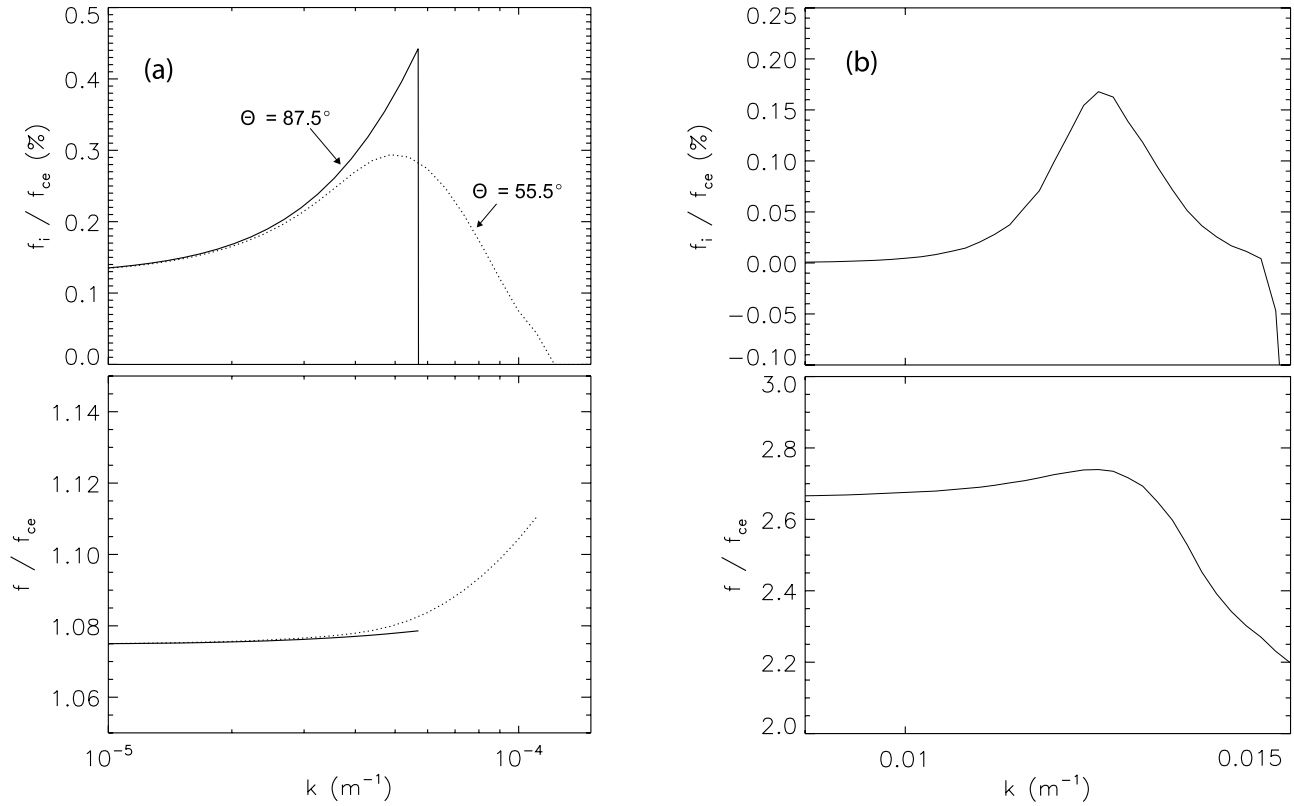
Figure 7. Real frequency (bottom plots) and growth rate (top plots) obtained from the linear dispersion analysis for the (a) fundamental and (b) harmonic emission centered near 9 kHz. Fundamental emission near peak growth at wave normal angle, $\theta = 87.5°$ (solid), and weaker but more broadbanded emission for $\theta = 55.5°$ (dotted) are shown. Harmonic emission in Figure 7b is calculated for $\theta = 88.0°$.

3.2. *Z* Mode and *O* Mode Growth Rate Calculations

[20] To determine the temporal growth/damping rates for magnetoionic (cold-plasma) modes under weakly relativistic formalism, we first discuss the dispersion relation for cold-plasma high-frequency modes. The discussion is similar to that given by *Stix* [1992] or by *Benson et al.* [2006]. The theoretical formulation is given as follows: First, the indices of refraction for X/Z and O/W modes (X is the extraordinary mode and W is the whistler mode) are given by

$$N_X^2 = 1 - \frac{\omega_p^2}{\omega(\omega + \tau\Omega)}, \qquad N_O^2 = 1 - \frac{\tau\omega_p^2}{\omega(\tau\omega - \Omega\cos^2\theta)}, \quad (2)$$

respectively, where

$$\tau = \left(s + \sqrt{s^2 + \cos^2\theta}\right)\frac{\omega_p^2 - \omega^2}{\left|\omega_p^2 - \omega^2\right|}, \qquad s = \frac{\omega\Omega\sin^2\theta}{2\left|\omega_p^2 - \omega^2\right|}, \quad (3)$$

and the frequency ranges for X/Z and O/W modes are specified by

$$\omega_X < \omega \quad \text{(fast } X \text{ mode)}, \qquad \omega_Z < \omega < \omega_Z^{res} \quad (Z \text{ mode}),$$
$$\omega_p < \omega \quad \text{(fast } O \text{ mode)}, \qquad 0 < \omega < \omega_W^{res} \quad (W \text{ mode)}. \quad (4)$$

Here the various cutoff and resonance frequencies are defined by

$$\omega_X = \frac{1}{2}\left(\sqrt{\Omega^2 + 4\omega_p^2} + \Omega\right), \quad \omega_Z = \frac{1}{2}\left(\sqrt{\Omega^2 + 4\omega_p^2} - \Omega\right),$$

$$\omega_Z^{res} = \frac{1}{\sqrt{2}}\left[\omega_p^2 + \Omega^2 + \sqrt{\left(\omega_p^2 - \Omega^2\right)^2 + 4\omega_p^2\Omega^2\sin^2\theta}\right]^{1/2}, \quad (5)$$

$$\omega_W^{res} = \frac{1}{\sqrt{2}}\left[\omega_p^2 + \Omega^2 - \sqrt{\left(\omega_p^2 - \Omega^2\right)^2 + 4\omega_p^2\Omega^2\sin^2\theta}\right]^{1/2}.$$

We plot the square of the index of refraction versus normalized frequency (ω/Ω) for these modes for a range of

Table 2. Comparison of Observed and Model Emissions

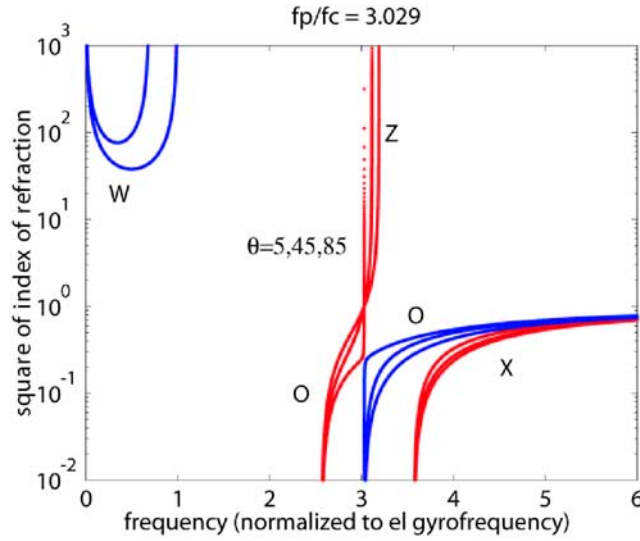|	EC Fundamental (Hz)	EC 1st Harmonic (Hz)
Observed bandwidth (Hz)	3650–4800	8500–9800
Calculated bandwidth (Hz) $\Delta\theta$	3650–4045 (55.5°–87.5°)	8315–9970 (88.0°–89.5°)

Figure 8. The square of the index of refraction versus normalized frequency for the X (extraordinary), W (whistler), O, and Z modes for a range of wave normal angles ($5°$, $45°$, and $85°$). Note that the O and Z modes are nearly coincident for small wave normal angles ($\theta \lesssim 5°$).

wave normal angles $\theta = 5°$, $45°$, and $85°$ in Figure 8 for $\omega_p/\Omega = 3.029$ (as determined above). We do not explicitly consider the W mode in this work. Note that the index of refraction curve for the Z mode and O mode at $\theta = 5°$ are nearly coincident at $\omega = \omega_p$.

[21] Next, on the basis of the formalism described in the past by *Yoon et al.* [1996, 1998], the growth rate for X and O modes are given, respectively, by

$$\gamma_X = \frac{\omega_p^2}{\omega} \frac{\pi^2}{R_X} \sum_{s=0}^{\infty} \left(\Theta(s\Omega - \omega) \int_{-1}^{1} d\mu Q_s^X(u+, \mu) \right.$$
$$\left. + \Theta(\omega - s\Omega)\Theta(1 - \mu_s^2) \int_{\mu_s}^{1} d\mu \sum_{+,-} Q_s^X(u\pm, \mu) \right),$$

$$\gamma_O = \frac{\omega_p^2}{\omega} \frac{\pi^2}{R_O} \sum_{s=0}^{\infty} \left(\Theta(s\Omega - \omega) \int_{-1}^{1} d\mu Q_s^O(u+, \mu) \right.$$
$$\left. + \Theta(\omega - s\Omega)\Theta(1 - \mu_s^2) \int_{\mu_s}^{1} d\mu \sum_{+,-} Q_s^O(u\pm, \mu) \right),$$

(6)

where

$$Q_s^X(u, \mu) = \frac{\tau^2}{\tau^2 + \cos^2\theta} \frac{u^2(1 - \mu^2)}{|u - N_X\mu\cos\theta|}$$
$$\cdot \left[\frac{\omega}{\Omega} \left(K_X \sin\theta + \frac{\cos\theta}{\tau}(\cos\theta - N_X u\mu) \right) \frac{J_s(b)}{b} + J_s'(b) \right]^2$$
$$\times \left(u \frac{\partial}{\partial u} + (N_X u\cos\theta - \mu)\frac{\partial}{\partial\mu} \right) f(u, \mu).$$

$$Q_s^O(u, \mu) = \frac{1}{\tau^2 + \cos^2\theta} \frac{u^2(1 - \mu^2)}{|u - N_O\mu\cos\theta|}$$
$$\cdot \left(\frac{\omega}{\Omega}[K_O\sin\theta\cos\theta - \tau(\cos\theta - N_O u\mu)] \frac{J_s(b)}{b} + \cos\theta J_s'(b) \right)^2$$
$$\times \left(u \frac{\partial}{\partial u} + (N_O u\cos\theta - \mu)\frac{\partial}{\partial\mu} \right) f(u, \mu).$$

(7)

and $u = \dfrac{p}{m_e c}$ is normalized momentum and $\mu = \dfrac{p_z}{p}$ is the cosine of the pitch angle.

[22] Various quantities that appear in (6) and (7) are defined by

$$u\pm = N_\sigma\mu\cos\theta \pm \sqrt{N_\sigma^2\mu^2\cos^2\theta + 2\left(\frac{s\Omega}{\omega} - 1\right)},$$

$$\mu_s = \frac{\sqrt{2}}{N_\sigma}\cos\theta\left(1 - \frac{s\Omega}{\omega}\right)^{1/2}, \qquad b_\pm = \frac{\omega}{\Omega}N_\sigma\sin\theta u \pm (1 - \mu)^{1/2},$$

$$K_X = \frac{\omega_p^2}{\omega_p^2 - \omega^2}\frac{\Omega\sin\theta}{\omega + \tau\Omega}, \qquad K_O = \frac{\omega_p^2}{\omega_p^2 - \omega^2}\frac{\tau\Omega\sin\theta}{\tau\omega - \Omega\cos^2\theta},$$

$$T_X = \frac{\cos\theta}{\tau}, \qquad T_O = -\frac{\tau}{\cos\theta},$$

$$R_X = 1 + \frac{\omega_p^2\left(\tau^2\omega^2 - \omega_p^2\cos^2\theta\right)}{\omega^2(\omega + \tau\Omega)^2\sin^2\theta}\frac{\tau^2 - \cos^2\theta}{\tau^2 + \cos^2\theta},$$

$$R_O = 1 + \frac{\omega_p^2\cot^2\theta\left(\tau^2\omega_p^2 - \omega_p^2\cos^2\theta\right)}{\omega^2(\tau\omega - \Omega\cos^2\theta)^2}\frac{\tau^2 - \cos^2\theta}{\tau^2 + \cos^2\theta}.$$

(8)

[23] In order to facilitate the analytical calculation of the growth rate of Z mode and O mode we introduce a functional form different from that of equation (1) for the electron distribution function as follows:

$$f(u, \mu) = \frac{1}{A}\left[\frac{r_0}{\pi^{3/2}\alpha_0^3}e^{-u^2/\alpha_0^2} + \frac{r_l}{\pi^{3/2}\alpha^3}e^{-u^2/\alpha^2} \right.$$
$$\cdot\left(1 + \Delta - \tanh\frac{u^2 - \mu_0^2}{\delta^2}\right) + \frac{r_b}{\pi^{3/2}\alpha_\perp^2\alpha_\parallel}$$
$$\left. \cdot e^{-u^2(1-\mu^2)/\alpha_\perp^2}\left(e^{-(u\mu-u_0)^2/\alpha_\parallel^2} + e^{-(u\mu-u_0)^2/\alpha_\parallel^2}\right) \right],$$

(9)

$$A = r_l\left(1 + \Delta - \delta\int_0^{1/\delta} dx\tanh\left(x^2 - x_0^2\right)\right) + 1 - r_l$$

$$r_0 = 1 - r_l - r_b, \qquad x_0 = \frac{\mu_0}{\delta}$$

where α_0 and α are the normalized thermal velocities of the background and energetic populations, respectively. We define $\mu_0 = \cos(\theta_L)$ where θ_L is the loss cone. The parameters δ and Δ determine the width and depth of the loss cone. This functional form incorporates a core distribution, r_0, energetic or loss cone population, r_l, and beam components, r_b.

[24] The parameters obtained for the functional form of equation (1) can be translated into the dimensional parameters of the model distribution function (9). The core electrons are characterized by thermal velocity, $v_T = 4.63 \times 10^6$ m/s. This is equivalent to $\alpha_0 \approx 0.0145$. The loss cone electrons have thermal speed 1.72×10^7 m/s, which gives $\alpha \sim 0.0573$. The number density of the energetic loss-cone electrons versus the total electrons is about 0.223. The loss-cone angle θ_L is about 20 degrees, which means $\mu_0 = \cos(\theta_L) \approx 0.9397$. The loss-cone depth is characterized in the model distribution by $\Delta \approx 3$. The beam drift speed is 3.727×10^6 m/s, which means $u_0 \approx 0.0124$. The beam thermal speed (defined in parallel direction) is 1.16×10^6 m/s, which makes
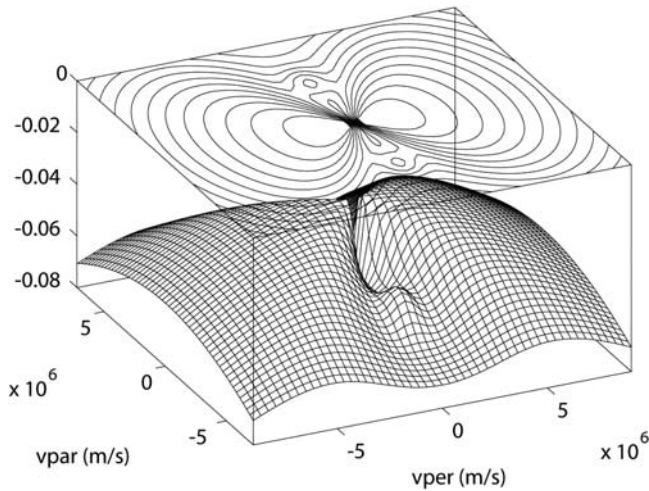
Figure 9. A 3-D plot of the model electron distribution function that corresponds to the functional form of equation (9) with the fitting parameters listed in the text. Note the general characteristics of a loss cone and low-energy counterstreaming beams.

$\alpha_{\parallel} \sim 0.0039$. The beam anisotropy factor is $T_{\perp}/T_{\parallel} \approx 0.529$, so that $\alpha_{\perp} = \sqrt{0.529}\,\alpha_{\parallel} \sim 0.0028$. Finally, the beam density defined with respect to the total density is 6.445×10^{-3} times 2. In Figure 9 we plot the model electron distribution without the core component, and in Figure 10 in 2-D we plot contours of the distribution including the core population, for direct comparison with Figure 4.

[25] Results of the growth rate calculations based upon the model distribution and input parameters are shown in Figures 11 and 12. Figure 11 shows the contours of Z and O mode growth rates against the propagation angle θ (Figure 11, left) and normalized frequency ω/Ω (Figure 11, right).

[26] Figure 12 (left) is a combined plot of growth rate contours for Z and O modes. Note the Z mode emission is narrowbanded. Figure 12 (right) shows the peak growth rates for O and Z mode versus ω/Ω. The vertical axis is in logarithmic scale, which shows that the O mode growth rate is many orders of magnitude lower than that of the Z mode. However, Z mode is a trapped mode that cannot readily escape the source region, unless it converts to O mode. Therefore, satellite observation of O mode may be locally generated Z mode that has converted to O mode [cf. *Yoon et al.*, 1998].

4. Discussion and Summary

[27] Next to Saturn kilometric radiation (SKR), Saturn narrowband emission is perhaps the most common and intense of the radio emissions observed at Saturn. In this study we have isolated an example of this emission at ~10 kHz near a fortuitous encounter by Cassini of a probable source region, and we study the possible wave generation mechanisms. For this case we have been fortunate to obtain electron phase space densities with a sufficient pitch angle distribution for analysis. The narrowband emission is commonly associated with ECH and upper hybrid (UH) emission. We perform a nonlinear least squares fit of the observed electron distribution to a sum of Maxwellians (equation (1)) and use the WHAMP dispersion solver to show that a loss cone distribution is the free energy source for the ECH emission. In order to estimate the emission gain for the ECH emission we note that the fundamental EC emission is ~25 dB above background, and the group velocity at the frequency of peak growth rate is $\sim 1.1 \times 10^{6}$ m/s. The path length required to obtain this gain is ~ 350 km. These waves are propagating at oblique angles with respect to the magnetic field (~20°) at frequencies near maximum growth.

[28] In addition to the analysis of growth of the ECH and UH emission, we use the theory of the cyclotron maser instability and a tractable analytic model of the electron distribution function (equation (9) and Figures 9 and 10) to calculate the wave growth rate for both Z mode and O mode narrowband emission. This is possible because, as discussed by *Yoon et al.* [1998], when the local upper hybrid frequency is in close vicinity to $2 f_{ce}$ or $3 f_{ce}$, harmonic Z mode emission growth rate can be exceedingly high. Our results indicate that the Z mode emission has a peak growth rate that is many orders of magnitude larger than the O mode (Figure 12). To account for the observed O mode narrowband emission seen in Figures 1c and 2 we postulate a mode conversion from Z mode to O mode near the satellite location at 1835 UT. Using the measured plasma parameters for this event we see from Figure 8 that the dispersion curves for the Z mode and O mode are nearly coincident for a wave normal angle of 5° for each mode. These results therefore indicate that a likely source of the observed narrowband emission is mode conversion of Z mode to O mode near the density gradient (indicated by the falling magnitude of f_{UH} seen in Figures 1c and 2)
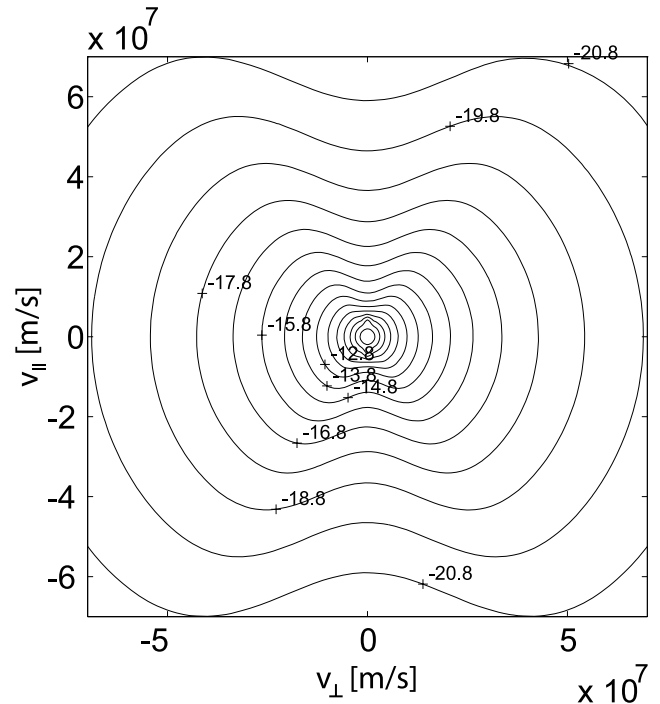

Figure 10. A 2-D plot of the model distribution function based on equation (9) for comparison to Figures 4 and 5. The contour levels are again in units of s^3/m^6.
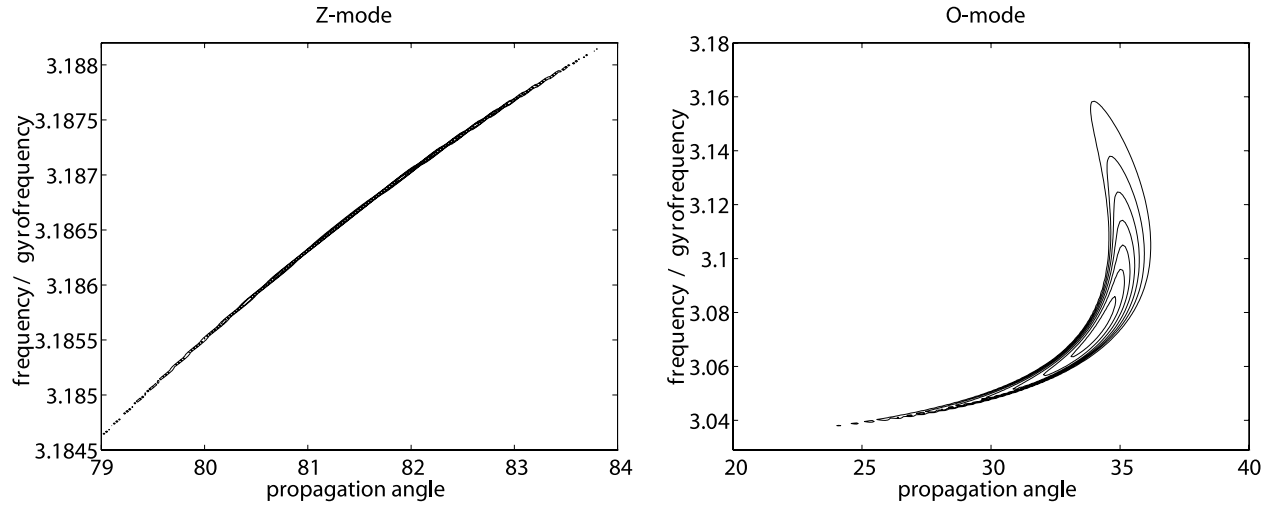
Figure 11. Contours of the temporal growth rates of the Z and O modes versus normalized frequency and wave normal angle.

where the index of refraction of the two modes match. Refraction of Z mode to small wave normal angles due to the density gradient allows the index of refraction to approach that of the O mode and facilitate mode conversion to O mode (NB) emission.

5. Conclusions

[29] The generation of ECH and UH emissions observed near source regions of narrowband emission can be explained by loss-cone free energy directly observed in the electron plasma pitch-angle distributions. Our results are consistent with the indirect generation of electromagnetic narrowband emission. The observed electron distribution is unstable to the direct generation of Z mode emission, which can then mode convert to O mode narrowband emission near the strong density gradient [cf. *Yoon et al.*, 1998]. The Saturn narrowband emission is similar in morphology to terrestrial continuum emission and to Jovian nKOM emission. The results of the analysis and theory presented

suggest its feasibility at other planets. It will be important to test this scenario for other encounters with source regions of narrowband emission, especially for conditions of varying ratios of f_p/f_{ce}.

References

Barbosa, D. D. (1982), Low-level VLF and LF radio emissions observed at Earth and Jupiter, *Rev. Geophys.*, *20*, 316–334.
Benson, R. F., P. A. Webb, J. L. Green, D. L. Carpenter, V. S. Sonwalkar, H. G. James, and B. W. Reinisch (2006), Active wave experiments in space plasmas: The Z mode, in *Geospace Electromagnetic Waves and Radiation*, edited by J. W. LaBelle and R. A. Treumann, Springer, Berlin.
Brown, L. W. (1973), The galactic radio spectrum between 130 kHz and 2600 kHz, *Astrophys. J.*, *180*, 359–370.
Budden, K. G. (1980), The theory of radio windows in the ionosphere and magnetosphere, *J. Atmos. Terr. Phys.*, *42*(3), 287–298.
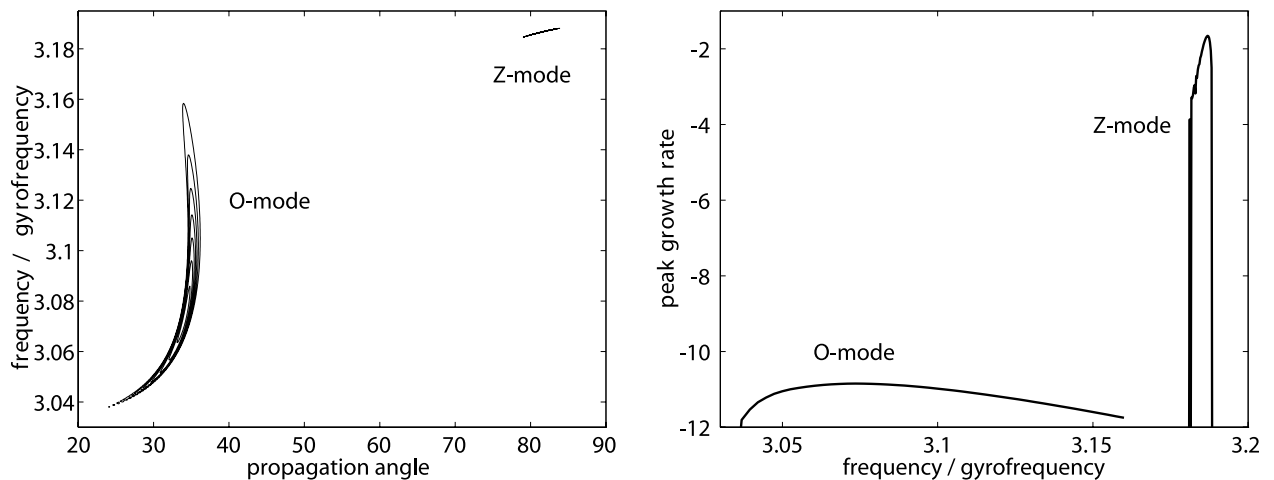

Figure 12. (left) Contours of the growth rate of the Z and O modes (from Figure 11). (right) Peak growth rates relative to Ω_{ce} for O and Z modes versus f/f_{ce}.

Connerney, J. E. P., M. H. Acuna, and N. F. Ness (1983), Currents in Saturn's magnetosphere, *J. Geophys. Res.*, *88*, 8779–8789.

Daigne, G., and Y. Leblanc (1986), Narrow-band Jovian kilometric radiation: Occurrence, polarization, and rotation period, *J. Geophys. Res.*, *91*, 7961–7969.

Ellis, G. R. (1956), The Z propagation hole in the ionosphere, *J. Atmos. Terr. Phys.*, *8*, 43–54.

Fischer, G., S.-Y. Ye, D. A. Gurnett, W. S. Kurth, and Z. Wang (2008), On the polarization of Saturn narrowband radio emissions, *Geophys. Res. Abstr.*, *10*, Abstract 04420.

Fung, S. F., and K. Papadopoulos (1987), The emission of narrow-band Jovian kilometric radiation, *J. Geophys. Res.*, *92*, 8579–8593.

Gurnett, D. A. (1974), The Earth as a radio source: Terrestrial kilometric radiation, *J. Geophys. Res.*, *79*, 4227–4238.

Gurnett, D. A. (1975), The Earth as a radio source: The nonthermal continuum, *J. Geophys. Res.*, *80*, 2751–2763.

Gurnett, D. A., and A. Bhattacharjee (2005), *Introduction to Plasma Physics*, pp. 123–126, Cambridge Univ. Press, Cambridge, U. K.

Gurnett, D. A., and R. R. Shaw (1973), Electromagnetic radiation trapped in the magnetosphere above the plasma frequency, *J. Geophys. Res.*, *78*, 8136–8149.

Gurnett, D. A., W. S. Kurth, and F. L. Scarf (1981), Narrowband electromagnetic emissions from Saturn's magnetosphere, *Nature*, *292*, 733–737.

Gurnett, D. A., W. S. Kurth, and F. L. Scarf (1983), Narrowband electromagnetic emissions from Jupiter's magnetosphere, *Nature*, *302*, 385–388.

Gurnett, D. A., et al. (2004), The Cassini Radio and Plasma Wave Investigation, *Space Sci. Rev.*, *114*(1–4), 395–463, doi:10.1007/s11214-004-1434-0.

Horne, R. B (1989), Path-integrated growth of electrostatic waves: The generation of terrestrial myriametric radiation, *J. Geophys. Res.*, *94*, 8895–8909.

Horne, R. B. (1990), Narrow-band structure and amplitude of terrestrial myriametric radiation, *J. Geophys. Res.*, *95*, 3925–3932.

Jones, D. (1976), Source of terrestrial non-thermal continuum radiation, *Nature*, *260*, 686–689.

Jones, D. (1987), Io plasma torus and the source of Jovian narrow-band kilometric radiation, *Nature*, *327*, 492–495.

Jones, D. (1988), Planetary radio emissions from low magnetic latitudes: Observations and theories, in *Planetary Radio Emissions II*, edited by H. O. Rucker, S. J. Bauer, and B.-M. Pedersen, pp. 255–293, Austrian Acad. of Sci. Press, Graz, Austria.

Kaiser, M. L., and M. D. Desch (1980), Narrow-band Jovian kilometric radiation: A new radio component, *J. Geophys. Res.*, *7*, 389–392.

Kurth, W. S. (1982), Detailed observations of the source of terrestrial narrowband electromagnetic radiation, *Geophys. Res. Lett.*, *9*, 1341–1344.

Kurth, W. S. (1992), Continuum radiation in planetary magnetospheres, in *Planetary Radio Emissions III*, edited by H. O. Rucker, S. J. Bauer, and M.-L. Kaiser, pp. 329–350, Austrian Acad. of Sci. Press, Graz, Austria.

Kurth, W. S., J. D. Craven, L. A. Frank, and D. A. Gurnett (1979a), Intense electrostatic waves near the upper hybrid resonance frequency, *J. Geophys. Res.*, *84*, 4145–4164.

Kurth, W. S., M. Ashour-Abdalla, L. A. Frank, C. F. Kennel, D. A. Gurnett, D. D. Sentman, and B. G. Burek (1979b), A comparison of intense electrostatic waves near f_{UHR} with linear instability theory, *Geophys. Res. Lett.*, *6*, 487–490.

Kurth, W. S., D. A. Gurnett, and R. R. Anderson (1981), Escaping nonthermal continuum radiation, *J. Geophys. Res.*, *86*, 5519–5531.

Melrose, D. B. (1981), A theory for the nonthermal radio continua in the terrestrial and Jovian magnetospheres, *J. Geophys. Res.*, *86*, 30–36.

Melrose, D. B. (1991), Emission at cyclotron harmonics due to coalescence of Z-mode waves, *Astrophys. J.*, *390*, 256–267.

Morgan, D. D., and D. A. Gurnett (1991), The source location and beaming of terrestrial continuum radiation, *J. Geophys. Res.*, *86*, 9595–9613.

Ronnmark, K. (1983a), Computation of the dielectric tensor of a Maxwellian plasma, *Plasma Phys.*, *25*, 699–701.

Ronnmark, K. (1983b), Emission of myriametric radiation by coalescence of upper hybrid waves with low frequency waves, *Ann. Geophys.*, *1*, 187–192.

Ronnmark, K. (1989), Myriametric radiation and the efficiency of linear mode conversion, *Geophys. Res. Lett.*, *16*, 731–738.

Ronnmark, K., H. Borg, P. J. Christiansen, M. P. Gough, and D. Jones (1978), Banded electron cyclotron harmonic instability—A first comparison of theory and experiment, *Space Sci. Rev.*, *22*, 401–417.

Santolik, O., and M. Parrot (1996), The wave distribution function in a hot magnetospheric plasma: The direct problem, *J. Geophys. Res.*, *101*(A5), 10,639–10,651.

Scarf, F. L., D. A. Gurnett, W. S. Kurth, and R. L. Poynter (1982), Voyager-2 plasma-wave observations at Saturn, *Science*, *215*, 587–594.

Stix, T. H. (1992), *Waves in Plasmas*, 556 pp., Am. Inst. of Phys., New York.

Wang, Z., D. A. Gurnett, W. S. Kurth, S.-Y. Ye, D. G. Mitchell, J. F. Carbary, and C. T. Russell (2008), Narrowband radio emissions and their relationship to rotating plasma clouds and magnetic disturbances at Saturn, *Geophys. Res. Abstr.*, *10*, Abstract 1216.

Warwick, J. W., et al. (1979), Planetary radio astronomy observations from Voyager 2 near Jupiter, *Science*, *206*, 991–995.

Willes, A. J., S. D. Bale, and Z. Kuncic (1998), A Z-mode electron-cyclotron maser model for bottomside ionosphere harmonic radio emissions, *J. Geophys. Res.*, *103*, 7017–7026.

Wu, C. S., and L. C. Lee (1979), A theory of the terrestrial kilometric radiation, *Astrophys. J.*, *230*, 621–626.

Ye, S., D. A. Gurnett, G. Fischer, B. Cecconi, J. D. Menietti, W. S. Kurth, Z. Wang, G. B. Hospodarsky, P. Zarka, and A. Lecacheux (2009), Source locations of narrowband radio emissions detected at Saturn, *J. Geophys. Res.*, doi:10.1029/2008JA013855, in press.

Yoon, P. H., A. T. Weatherwax, T. J. Rosenberg, and J. LaBelle (1996), Lower ionospheric cyclotron maser theory: A possible source of $2 f_{ce}$ and $3 f_{ce}$ auroral radio emissions, *J. Geophys. Res.*, *101*, 27,015–27,025.

Yoon, P. H., A. T. Weatherwax, T. J. Rosenberg, J. LaBelle, and S. G. Shepherd (1998), Propagation of medium frequency (1–4 MHz) auroral radio waves to the ground via the Z-mode radio window, *J. Geophys. Res.*, *103*, 29,267–29,275.

Young, D. T., et al. (2004), Cassini plasma spectrometer investigation, *Space Sci. Rev*, *114*, 1–112.

———————————

A. J. Coates, Mullard Space Science Laboratory, University College London, Dorking RH5 6NT, UK. (ajc@mssl.ucl.ac.uk)

D. A. Gurnett, J. D. Menietti, and S.-Y. Ye, Department of Physics and Astronomy, University of Iowa, Van Allen Hall, Iowa City, IA 52242-1479, USA. (john-menietti@uiowa.edu; shengyi-ye@uiowa.edu)

A. M. Rymer, Applied Physics Laboratory, Johns Hopkins University, Laurel, MD 20707, USA. (abigail.rymer@jhuapl.edu)

O. Santolik, Faculty of Mathematics and Physics, Charles University, Prague, Czech Republic. (ondrej.santolik@mff.cuni.cz)

P. H. Yoon, Institute for Physical Science and Technology, University of Maryland, College Park, MD 20742, USA. (yoon@ipst.umd.edu)